MMPhU-Net: A Novel Multi-Model Fusion Phase Unwrapping Network for Large-Gradient Subsidence Deformation

Yandong Gao, Jiaqi Yao, Nanshan Zheng, Shijin Li, Hefang Bian, and Yu Tian

***Abstract*—The problem of phase unwrapping (PhU) in the large-gradient deformation areas is the bottleneck problem of interferometric synthetic aperture radar (InSAR) data processing. However, the extraction of large-gradient deformation areas is one of the key issues in coal mining deformation monitoring. Here, we propose a novel multimodel fusion PhU Network, abbreviated as MMPhU-Net, and apply it to the extraction of large-gradient deformation areas. The major advantages of MMPhU-Net are as follows: First, MMPhU-Net combines the advantages of different basic network models, which can improve the model convergence speed and phase gradient estimation accuracy. MMPhU-Net can improve the lack of recognition effect of a single basic model. Second, different from existing deep learning PhU methods, MMPhU-Net directly estimates the gradient ambiguity numbers, k, so its phase gradient estimation completely breaks through the $(-\pi, \pi)$ limitation. Therefore, MMPhU-Net can obtain ideal PhU results in large-gradient deformation areas. In addition, optimization algorithm models are used to optimize the estimation results of the multimodel fusion network. Subsequently, the obtained k and a novel two-step filtering method are combined to obtain the final PhU results. Through the verifications of simulated data sets and realistic GaoFen-3 SAR data sets, the proposed MMPhU-Net method can achieve superior excellent results than the commonly used PhU method.**

***Index Terms*—Interferometric synthetic aperture radar (InSAR), large-gradient deformation areas, phase unwrapping (PhU), the multimodel fusion network, two-step filtering (TSF).**

I. Introduction

INTERFEROMETRIC synthetic aperture radar (InSAR) has been widely used in topographic mapping [1], urban safety development [2] and coal mining subsidence monitoring [3]. Differential InSAR (DInSAR) is an effective coal mining safety monitoring method. DInSAR uses radar satellites to obtain the phases of the same monitoring area at two different times, and then performs differential interferometric phases to obtain deformation information [4], [5]. DInSAR can obtain the deformation of mining subsidence with high efficiency and high precision, so it has been favored in practical engineering applications [6]. However, the complexity of coal mining conditions and the diversity of subsidence changes make DInSAR subject to many restrictions in mining subsidence monitoring. The extraction of large-gradient deformation has become one of the key issues of DInSAR in mining subsidence monitoring [7]. The large-gradient deformation areas can violate the phase continuity assumption, and the interferometric fringes are prone to mixing. Therefore, the large-gradient deformation areas will affect the phase unwrapping (PhU) accuracy, and even lead to PhU failure [8], [9]. As we all know, the accuracy of PhU is critical to obtain the final DInSAR deformation product [10]. However, in many coal mining subsidence monitoring processes, it is challenging to obtain the deformation of the coal mine collapse center [11], [12].

In recent years, numerous researchers have conducted extensive studies on the extraction of large-gradient deformation in coal mining subsidence, categorically classified into three main groups [13]. Wu et al. [14] used the raised cosine interpolation algorithm to perform interpolation and resampling on the SAR image before the interferometric processing. However, obtains the estimation of the subsidence center through interpolation algorithm cannot fundamentally resolve the challenge of extracting areas with significant deformation gradients. Ng et al. [15] proposed a method for extracting large-gradient deformations in mining areas, which combines three different imaging modes. However, this method is limited by different satellite imaging modes. Some scholars applied offset-tracking to the extraction of large-gradient deformation areas [16], [17]. Chen et al. [18] applied the combination of SBAS and offset tracking to coal mining large-gradient deformation extraction, and combined the data of two different sensors to perform experiments, which can obtain optimal outcomes in areas with large-gradient deformation. Huang et al. [19] proposed an advanced pixel tracking technique for monitoring large-gradient deformation in subsidence caused by mining. Unfortunately, the accuracy of offset-tracking is low, which is only 1/10 $\sim$ 1/20 of the pixel resolution [20]. The second category is to

Manuscript received 10 December 2023; revised 3 January 2024; accepted 25 January 2024. Date of publication 8 February 2024; date of current version 26 February 2024. This work was supported in part by the National Natural Science Foundation of China under Grant U22A20569, Grant 42001409, and Grant 42271460 and in part by the State Key Program of China Postdoctoral Science Foundation under Grant 2023M733743. *(Corresponding authors: Jiaqi Yao; Nanshan Zheng.)*

Yandong Gao, Nanshan Zheng, Shijin Li, Hefang Bian, and Yu Tian are with the School of Environment and Spatial Informatics, China University of Mining and Technology, Xuzhou 221116, China (e-mail: ydgao@cumt.edu.cn; znshcumt@cumt.edu.cn).

Jiaqi Yao is with the Academy of Eco-civilization development for Jing-Jin-Ji megalopolis, Tianjin Normal University, Tianjin 300387, China (e-mail: yaojiaqi@tjnu.edu.cn).

Digital Object Identifier 10.1109/JSTARS.2024.3362389

© 2024 The Authors. This work is licensed under a Creative Commons Attribution-NonCommercial-NoDerivatives 4.0 License. For more information, see https://creativecommons.org/licenses/by-nc-nd/4.0/

combine other deformation monitoring technologies to obtain the deformation of mining subsidence with significant gradients. Bingqian et al. [21] proposed a method that combines SAR data with three-dimensional (3-D) laser scanning point cloud data to extract significant deformations in mining subsidence with large gradients. Yang et al. [22] proposed a method that integrates InSAR with level to analyze the dynamic subsidence of the mining subsidence. However, the acquisition of the data required by these methods is difficult. In addition, the accuracy of these techniques is often lower than that of InSAR measurements. The third category has always been considered the most commonly used method, which applies the mining subsidence model to the extraction of large-gradient deformation areas. Jiang et al. [23] proposed an InSAR 3-D surface deformation extraction method that relies on the dynamic probabilistic integration PhU method. Diao et al. [11] suggested a prediction-based PhU technique that mitigates PhU errors at the coal mining subsidence center, improves the accuracy of the PhU, and obtains large-gradient deformation in the subsidence caused by coal mining. Yang et al. [13], [24] conducted in-depth research on the problem of mining subsidence probability integral prediction model, and proposed a series of parameter optimization methods. These methods have obtained relatively ideal results in obtaining large-gradient deformation. Nevertheless, the deformation derived from these methods represents only model predictions, rather than actual and valid observations [25].

To summarize, the retrieval of substantial deformation gradients in coal mining subsidence remains a critical aspect of research and poses significant challenges [26]. The existing research shows that PhU has a great influence on this problem [27]. Generally speaking, PhU methods can be categorized into two main groups [28]. The first category is path-following methods that integrate along different paths to obtain unwrapped results [29]. This category of methods belong to the local optimization PhU methods. The second category is the optimization-based PhU methods represented by minimum cost flow, L^{P}-norm and statistical cost network-flow [30]. This category of methods belongs to the global optimization PhU methods. These methods have been widely used. However, the challenge of PhU in handling large-gradient changes remains a bottleneck issue [31]. Recently, deep learning has carried out relevant researches in the PhU problem [32], [33]. However, it is still not possible to get the ideal result in the large-gradient deformation [34], [35]. Fortunately, deep learning provides novel ideas for extracting large-gradient deformation in coal mining subsidence [36], [37], [38], [39].

For the bottleneck problem of existing PhU methods, here, we propose a novel multimodel fusion PhU Network, abbreviated as MMPhU-Net. Firstly, we examine the characteristics of deformation areas caused by mining subsidence. The distribution characteristics of gradient ambiguity numbers (k) are obtained through simulation data, and then the simulation data are used to establish the DInSAR simulation data sets required for deep learning. Then, the SegNet and U-Net jointly train the simulated data to obtain the k distribution maps of the deformation areas. In addition, test time augmentation (TTA) and conditional random field (CRF) are used to optimize the estimation results to obtain better k distribution maps. Finally, the final mining subsidence deformation results are obtained by combining the k distribution maps and a novel two-step filtering (TSF) method. The proposed MMPhU-Net method uses the deep learning method to directly extract the k. Therefore, more ideal results can be obtained in the large-gradient subsidence deformation areas. We use different forms of data sets to validate MMPhU-Net. The proposed MMPhU-Net can obtain more large-accuracy subsidence results than the existing PhU methods, especially in the areas with large-gradient subsidence deformation.

The rest of this article is organized as follows. In Section II, the processing of DInSAR coal mining deformation monitoring and PhU are reviewed. Subsequently, the proposed MMPhU-Net is introduced in Section III. In Section IV, the experimental analyses of different PhU methods are presented. Finally, Section V concludes this article.

II. DInSAR Processing and PhU Background

A. Review of DInSAR

The deformation value ΔR can be obtained by the following [2]:

$$\Delta R = -\frac{\lambda}{4\pi}\psi_{\mathrm{defo}} \tag{1}$$

where ψ_{defo} is the absolute phase, λ is the radar incident wavelength. Through (1) we can get ΔR. However, in the actual interferometric processing, the interferometric phase is composed of multiple phases. The phase can be expressed as follows:

$$\varphi = \varphi_{\mathrm{topo}} + \varphi_{\mathrm{defo}} + \varphi_{\mathrm{flat}} + \varphi_{\mathrm{atm}} + \varphi_{\mathrm{noise}} \tag{2}$$

where φ_{topo} is the topography information, φ_{defo} is the surface deformation, φ_{flat} is the flattened phase, φ_{atm} is the atmospheric error and φ_{noise} is the noise. With the help of digital elevation model (DEM), the differential phase $\Delta\varphi$ can be obtained by

$$\Delta\varphi = \varphi_{\mathrm{defo}} + \Delta\varphi_{\mathrm{topo\_e}} + \Delta\varphi_{\mathrm{orbit}} + \Delta\varphi_{\mathrm{atm}} + \Delta\varphi_{\mathrm{noise}} \tag{3}$$

where $\Delta\varphi_{\mathrm{topo\_e}}$ is the residual topography phase caused by the inaccuracy of DEM data and $\Delta\varphi_{\mathrm{orbit}}$ is the orbit error phase. These phase contributions can be weakened by theoretical formula calculation, model fitting, filtering and other methods. Furthermore, we can obtain the deformation phase through the differential phase. However, at this time, the true phase is wrapped in $[-\pi, \pi]$.

B. Mathematical Foundation of PhU

The relationship between ψ_{defo} and φ_{defo} is as follows:

$$\psi_{\mathrm{defo}} = \varphi_{\mathrm{defo}} + 2k\pi \tag{4}$$

where k represents the gradient ambiguity number. The phase gradient can be obtained by

$$\begin{aligned}\Delta\psi_{\mathrm{defo}}(s, s-1) &= \psi_{\mathrm{defo}}(s) - \psi_{\mathrm{defo}}(s-1) \\ &= \varphi_{\mathrm{defo}}(s) - \varphi_{\mathrm{defo}}(s-1) + 2\Delta k(s, s-1)\pi \\ &= \Delta\varphi_{\mathrm{defo}}(s, s-1) + 2\Delta k(s, s-1)\pi\end{aligned} \tag{5}$$

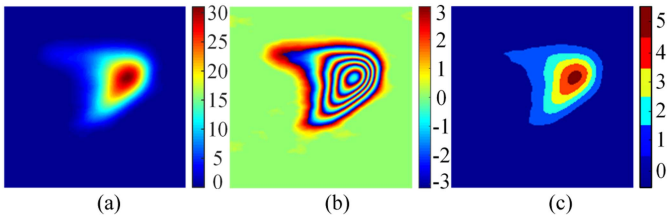

Fig. 1. (a) Simulated mining subsidence deformation absolute phase. (b) Interferogram of (a). (c) Gradient ambiguity numbers distribution map of (b).

where $\Delta\psi_{\text{defo}}(s, s-1)$ represents the unwrapped phase gradient, $\Delta\varphi_{\text{defo}}(s, s-1)$ is the wrapped phase gradient. Form (4) and (5), we can obtain

$$\begin{aligned}\psi_{\text{defo}}(s) &= \psi_{\text{defo}}(s-1) + \Delta\psi_{\text{defo}}(s, s-1) \\ &= \psi_{\text{defo}}(s-1) + \Delta\varphi_{\text{defo}}(s, s-1) + 2\Delta k(s, s-1)\pi. \quad (6)\end{aligned}$$

Consequently, we can obtain the ultimate deformation phase based on (6).The phase continuity assumption is a key premise of conventional 2-D PhU methods. The equation can be expressed in the following manner [8]:

$$\Delta\psi_{\text{defo}}(s, s-1) = \begin{cases} \varphi_{\text{defo}}(s) - \varphi_{\text{defo}}(s-1) & |\varphi_{\text{defo}}(s) - \varphi_{\text{defo}}(s-1)| \le \pi \\ \varphi_{\text{defo}}(s) - \varphi_{\text{defo}}(s-1) - 2\pi & \varphi_{\text{defo}}(s) - \varphi_{\text{defo}}(s-1) > \pi \\ \varphi_{\text{defo}}(s) - \varphi_{\text{defo}}(s-1) + 2\pi & \varphi_{\text{defo}}(s) - \varphi_{\text{defo}}(s-1) < -\pi \end{cases}. \quad (7)$$

According to (6) and (7), it can be seen that the commonly used PhU method $\Delta k(s, s-1)$ has a value of $0, \pm 1$. However, it is difficult to guarantee the value of $\Delta k(s, s-1)$ in areas characterized by large-gradient deformation caused by coal mine subsidence. Therefore, the existing PhU methods are difficult to obtain ideal results in coal mining large-gradient subsidence areas. It is one of the main factors limiting the extraction of large-gradient deformation areas in coal mining.

III. MMPhU-Net Method

A. Phase Gradient Ambiguity Estimation

According to (4), it is evident that the difference between the deformation wrapped and the true absolute phase is $2k\pi$. In the event that an accurate value for k can be obtained, the true phase can be accurately obtained. As shown in Fig. 1, it is evident that the simulated coal mining subsidence deformation interferogram and the corresponding k distribution map. The equation for obtaining k is as follows:

$$k = \text{round}\left(\frac{\psi_{\text{defo}} - \varphi_{\text{defo}}}{2\pi}\right) \quad (8)$$

where round$(\cdot)$ is the nearest integer operator. It can be seen from Fig. 1 that the k corresponding to different interferometric fringes are also different. The width of the fringes in the k map can be considered as a buffer for the change of the k. The k change buffer is smaller in the densely fringes area, and the k change buffer is larger in the sparsely fringes area. Therefore, even in the area of large gradient changes, if the k can be obtained, the accurate PhU results can be obtained. Deep learning can obtain the required data based on the characteristics of the data. Moreover, deep learning has been widely used in classification problems. Fortunately, through analysis, we found that the extraction of k can be converted into a classification problem. Therefore, we can use deep learning methods to obtain k without considering large-gradient deformation areas.

B. Introduction of Network Architecture

In this article, we obtain higher accuracy k by fusing multiple semantic segmentation models, which is named MMPhU-Net. The advantage of this MMPhU-Net is to speed up the model convergence and make the final detection results combine the advantages of multiple basic models. As shown in Fig. 2, the fusion model network used in this article is composed of U-Net and SegNet, and they are the classical network structures commonly used in remote sensing. The models acquire typical features of images by simple and efficient encoder-decoder. The models are mainly composed of convolutional layer, pooling layer, upsampling layer, soft-max layer, etc. [40], [41]. The U-Net used in this article is an improved U-shaped structured network based on FCN [42]. The encoding step is superimposed with the feature maps obtained by deconvolution in the corresponding decoding step, which in turn yields more refined category information. However, jagged contour noise is generated at the edges of the predicted k. SegNet is a symmetric structure with improved mapping of the deconvolution layer compared to FCN [43]. SegNet can improve the spatial continuity of the target image, but there is a certain degree of errors at the edge of the k map detection area. Therefore, in order to combine the respective characteristics of the two models, we perform model fusion (ensemble generation) by means of Adboosting. In addition, we post-processed the obtained k maps in order to obtain higher accuracy k maps. TTA and CRF are used in the post-processing process to optimize the detection effect of k maps [44], [45].

In this article, the model training experiment uses Tensorflow deep learning framework, which is a deep learning framework launched by Google in 2015. It encapsulates many deep learning tools at a high level, such as Estimator, Keras, etc., and provides good visualization functions [46]. In addition, the experiments in this article were run under the following environment: Windows, Intel(R) CPU E31505M v3 @ 2.3 Hz, graphics card NVIDIA Quadro K2200, and 128G RAM.

The training model process consists of three main parts: preprocessing, model fusion and postprocessing.

1) Preprocessing: It mainly contains three parts, such as data labeling, image segmentation and data broadening. As shown in Fig. 3, the simulated interferograms of different deformation areas are used as data samples and the corresponding k-distribution feature maps as data labels, which together form the initial training set. Considering the training environment, data prediction scale and other factors, the initial training set data are uniformly cropped into 64 × 64 size image blocks, and the number is increased to 10 000 by the data augmentation function to form the training set.

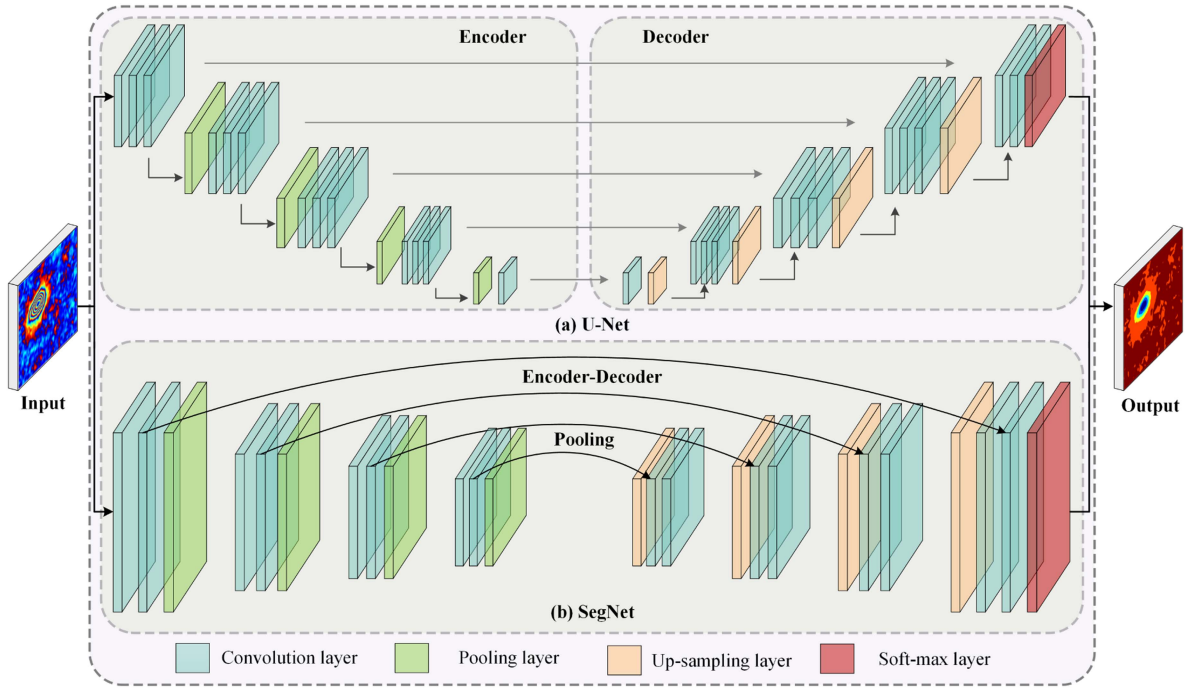

Fig. 2. Schematic diagram of multimodel fusion PhU network architecture. (a) U-Net model. (b) SegNet model.

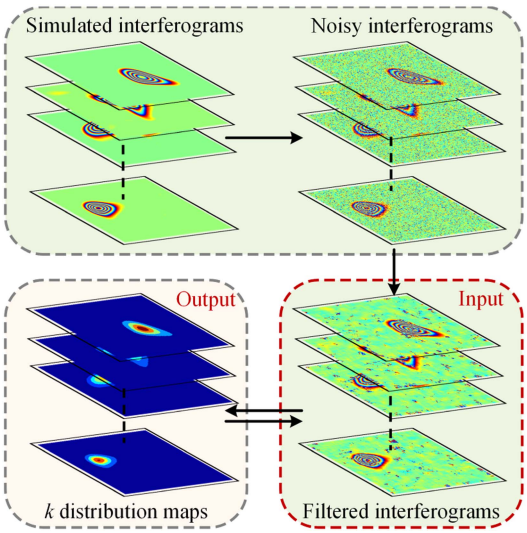

Fig. 3. Part of simulated mining subsidence deformation data used to train the model in this article.

2) Model Fusion: In the process of multiple rounds of iterative training, if the model recognizes the differences between categories and typical features within categories more significantly, the convergence speed of the model will be accelerated, the corresponding overall accuracy will also be improved, and the probability of missing detection and false detection will gradually be decreased. In this section, we uses the Adboosting algorithm is employed to realize the integration of multiple elementary models, thereby improving the accuracy of recognition. Adaboosting is a machine learning algorithm based on greedy theory to minimize the upper limit of the loss caused by wrong classification. In each iteration, the overall training efficiency is improved by reweighting the wrong samples of multiple weak classifiers. Quantify the error of the multibasic model in each round of training through the error loss function, as shown

$$\mathrm{Err}_m = \frac{\sum_{i=1}^{N} w_i P(y_i \neq G_m(x_i))}{\sum_{i=1}^{N} w_i} \tag{9}$$

where N is the categories of basic models($N = 2$), w_i is defined as $1/N$ at initialization. $G_m(x_i)$ is the classification result. $P(y_i \neq G_m(x_i))$ is the probability that the mth round of training the i th basic model predicts a classification error.

Then, based on the model fusion coefficient α_m calculated in the previous step, the reasonable estimation of the weight of each basic model is realized, as shown in

$$\alpha_m = \frac{1}{2} \log \frac{1 - \mathrm{Err}_m}{\mathrm{Err}_m}. \tag{10}$$

Finally, the initial weight of each basic model is redistributed based on the model fusion coefficient, and the next round of training is started after updating the parameters, as shown in (11). Through model fusion, we can improve training efficiency and combine the characteristics of different basic models

$$w_i(\text{update}) = w_i \cdot \exp(-\alpha_m \cdot P(y_i \neq G_m(x_i))). \tag{11}$$

3) Postprocessing: Although the model gradually converges and saturates in accuracy after several rounds of training and iterations, it is still possible to miss detection due to typical features being partially generalized, etc., just by inputting the images to be detected into the model. Therefore, it is necessary to post-process the images to be detected. This section mainly adopts two methods, TTA and CRF. The overall post-processing process is as follows.

a) The image to be detected is rotated, noise is added, etc..
b) The feature probability map output from the model is inverted by performing the geometric operation in step a) to recover the image plane coordinates of the image to be detected.
c) Summing and averaging the nine feature probability maps, and outputting the final results.
d) Using the original image and the final detection results as the input to the CRF, the classification results are corrected according to the energy function.

C. Correction of Unwrapped Results

The results accuracy of MMPhU-Net are higher, however, there will be a small amount of phase jumps at the intersection of different gradient ambiguity numbers. Therefore, we introduce a TSF method to correct the phase jumps and further improve the PhU results accuracy. The nonlocal means filtering (NLMF) method has superior edge preservation. Therefore, we use the NLMF method to initially correct the PhU results. Here is the equation

$$\psi'_{defo} = \frac{1}{\sum \omega} \sum_{(a,s)\in Q} \omega \cdot \psi_{defo}(a,s) \tag{12}$$

where ψ'_{defo} is the NLMF result, $\psi_{defo}(a,s)$ is the searched block, Q is the search scope, and ω is a weighted value, $0 \le \omega \le 1$. Traditional NLMF is less efficient. Therefore, we set the windows of searched phase block and Euclidean distance to 5×5 to improve the efficiency of NLMF. The smoothing factor is 10. So as to further improve the accuracy of PhU, we perform a quadratic correction on the residual phase, the equation is as follows:

$$\psi_{res} = \psi_{defo} - \psi'_{defo} \tag{13}$$

$$\psi'_{res} = \text{median} \sum_{(m,n)\in Q} \psi_{res}(m,n) \tag{14}$$

$$\hat{\psi}_{defo} = \psi'_{defo} + \psi'_{res} \tag{15}$$

where ψ_{res} is the filtered residual phase, $\psi_{res}(m,n)$ is the searched phase, and ψ'_{res} is the recovery phase of the residual phase. The first step of NLMF has achieved a good result. Therefore, the second step uses median filtering to correct the residual phase (window is 7×7) to obtain the loss phase. Finally, by (15) we can get the final deformation phase $\hat{\psi}_{defo}$. Form Fig. 4, it is apparent that the phase accuracy has been significantly improved after correction.

D. Generation of Training Data

The training data is reasonable or not is affecting the accuracy of the gradient ambiguity numbers obtained by the deep learning model. Therefore, in order to fully simulate the DInSAR mining subsidence deformation monitoring interferograms. We simulated 16 different subsidence deformation interferograms, and during the model training, these 16 deformation interferograms were deformed, stretched, and flipped to further increase the types of training data. Fig. 3 is part of simulated mining subsidence deformation data used in this article. The categories of simulated mining subsidence deformation interferograms used in this article are diversified. We use the filtering method of our previous research to filter the noisy interferograms (see [47]), and use the filtered interferograms as the input. According to (8), we can obtain the distribution maps of gradient ambiguity numbers and use them as the output. In summary, the schematic representation of the proposed method can be represented by Fig. 5.

1) *Step* 1: According to the deformation characteristics of the mining, the simulated data of the subsidence deformation are obtained. In addition, hypergeometric noise is added to the phase of simulated mining subsidence. In order to obtain more accurate simulation data, we filter the noisy interferograms, and use the filtered interferograms as the input of the learning model.

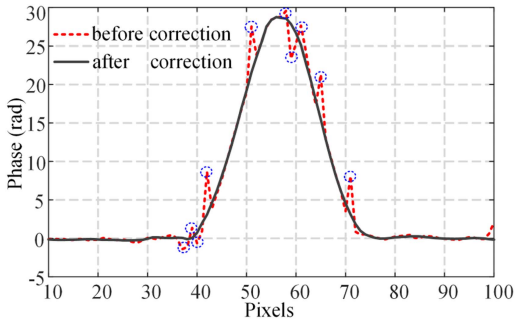

Fig. 4. Comparison of unwrapped phase profiles before and after correction.

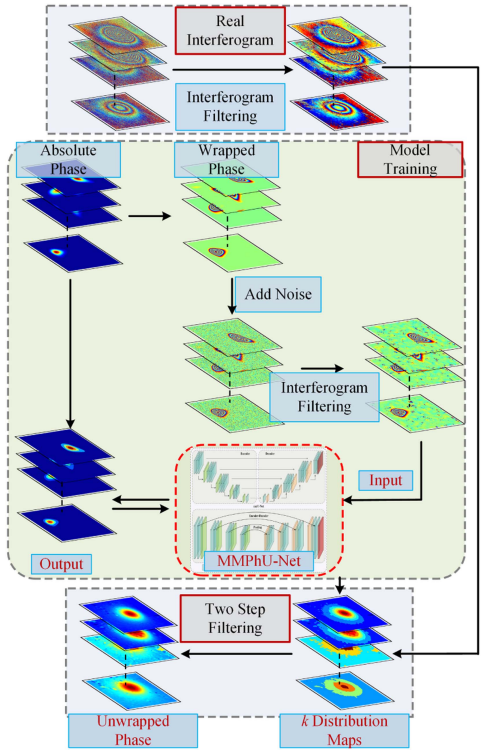

Fig. 5. Schematic representation of the proposed MMPhU-net method.

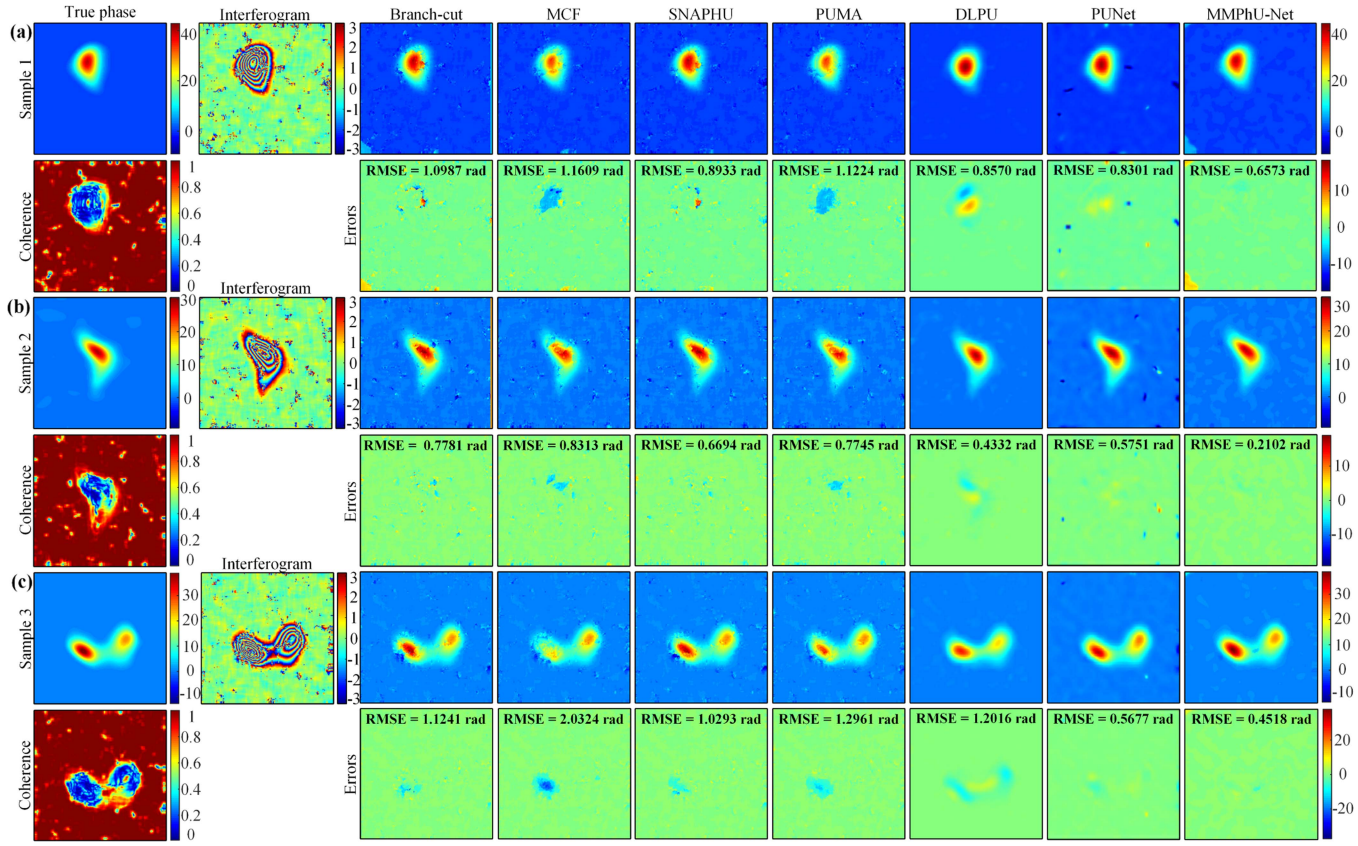

Fig. 6. Unwrapped results of simulated interferograms. (a) True phase, filtered interferogram, coherence map of sample 1, unwrapped results and unwrapped errors of different methods. (b) True phase, filtered interferogram, coherence map of sample 2, unwrapped results and unwrapped errors of different methods. (c) True phase, filtered interferogram, coherence map of sample 3, unwrapped results and unwrapped errors of different methods.

2) *Step* 2: According to (8), we can obtain the distribution maps of the k, and use them as the output. Based on this and step 1, the DInSAR mining subsidence deformation monitoring data set is established.
3) *Step* 3: According to step 2, we use DInSAR mining subsidence deformation monitoring data sets for training and validating the network. In addition, we combine TTA and CRF to optimize the training results. The accuracy of prediction results has been further improved.
4) *Step* 4: The realistic subsidence deformation interferograms are used as the input, and through step 3 we can obtain accurate gradient ambiguity numbers distribution maps. According to (4), we obtain the unwrapped deformation phase of the realistic data. To improve the accuracy even further, we introduce a TSF method to correct the unwrapped phase of the deformation, and obtain the final unwrapped results.
5) *Step* 5: According to the unwrapped phase obtained in step 4, we can further obtain the real subsidence deformation result of the mining area.

IV. Experiments and Discussion

In this section, we validate different PhU methods using the simulated DInSAR mining subsidence deformation data sets and the realistic SAR data sets. MMPhU-Net is compared with traditional model-driven methods, DLPU [48] and PUNet [36]. We use the root-mean-square-error (RMSE) to assess the simulation data results, which can be represented by the following equation:

$$\mathrm{RMSE} = \sqrt{\frac{\sum_{t=1}^{T} \left(\psi_t - \hat{\psi}_t\right)^2}{T}} \tag{16}$$

where T is the number of pixel, ψ_t represents the unwrapped phase, and $\hat{\psi}_t$ represents the true phase.

A. Validation Using Simulated Data

Three sets of simulated DInSAR mining subsidence deformation data are employed to examine the results of various PhU methods. Fig. 6(a) is the experimental data and results of sample 1. The filtered interferogram has a significant phase discontinuity, and the coherence of the deformation center is poor. Therefore, the results of MCF and PUMA produce noticeable unwrapped errors in the deformation centers. Although branch-cut and SNAPHU obtained ideal results in mining subsidence centers, obvious unwrapped errors occurred in discontinuous areas. DLPU seems to be able to obtain relatively ideal unwrapped results. However, it can be seen from the unwrapped errors that DLPU still produces phase loss in the deformation centers. Compared to previous methods, PUNet can achieve superior

unwrapped results. Unfortunately, the center of the subsidence deformation and its surrounding areas still produce obvious errors. The results of MMPhU-Net are closest to the true phase, especially in the center of subsidence deformation. MMPhU-Net can almost completely obtain the unwrapped phase of the mining subsidence center. It can be further verified from RMSEs that the MMPhU-Net method is the best among several methods. Moreover, the reason why the MMPhU-Net unwrapped result RMSE is 0.6573 rad is that the error is mainly generated at the edge of the interferogram, not the subsidence deformation area. Sample 2 is a mining subsidence area with relatively irregular deformation, and the filtered interferogram is relatively clear. However, MCF and PUMA still produce obvious errors in the mining subsidence centers, and the RMSEs of the errors are 0.8313 and 0.7745 rad, respectively. Similar to the experimental results of sample1, branch-cut and SNAPHU did not generate errors in the centers of the mining subsidence, but still produced obvious unwrapped errors at the edge of the subsidence deformation area, and the RMSEs of the unwrapped errors were 0.7781 and 0.6694 rad, respectively. The deep learning PhU methods have better robustness. Therefore, DLPU and PUNet can obtain superior unwrapped results compared to the previous methods. Although the RMSE of DLPU is only 0.4332 rad, unfortunately, DLPU still produces a relatively obvious unwrapped errors in the center of deformation. The unwrapped results of PUNet in the center of deformation are significantly better than DLPU. However, the RMSE of PUNet is 0.5751 rad, which still has obvious unwrapped errors in the deformation center and surrounding areas. MMPhU-Net can still obtain relatively favorable results, with a RMSE of the unwrapped error at only 0.2102 rad, representing the best result among several PhU methods. Sample 3 is a deformation area composed of two adjacent deformation. Moreover, the deformation characteristics are more complex, and the filtered interferogram produces serious phase discontinuity. It can be seen that all traditional model-driven PhU methods produce obvious unwrapped errors. In particular, MCF can hardly accurately obtain the phase of the center. The RMSEs of branch-cut, MCF, SNAPHU and PUMA are 1.1241d, 20.324, 1.0293, and 1.2961 rad, respectively. DLPU produced relatively obvious unwrapped errors at the center of the deformation, with a RMSE of 1.2016 rad. The RMSE of PUNet is 0.5677 rad, which is the best among the previous methods. However, a small amount of unwrapped errors is still produced in the deformation center area. It can be seen that the existing PhU methods have been unable to obtain ideal results. However, MMPhU-Net can almost completely obtain the phase of the mining deformation area, and the RMSE of unwrapped error is only 0.4518 rad, which further proves that the proposed MMPhU-Net is the best among several methods.

B. Validation Using Realistic Data

In this section, realistic mining subsidence deformation data sets of GaoFen-3 SAR are used to verify the performance of different PhU methods. Fig. 7(a) is the distribution map of realistic GaoFen-3 SAR data experiment. Fig. 7(b) is the DEM of the realistic data. Fig. 7(c)–(e) are the filtered interferograms in the red rectangle of Fig. 7(b). From Fig. 7(c), it is evident that a clear phase discontinuity exists in the center of the interferogram. The fringes in the central area of the interferogram in Fig. 7(d) produce severe aliasing. It can be seen from Fig. 7(e) that the interferometric fringes in the edge of the subsidence deformation are relatively clear, but there are obviously serious discontinuities in the deformation center. Fig. 8 are the experimental data of Fig. 7(c)–(e) and the results of different PhU methods. Fig. 8(a) is three sets of real data interferograms and coherence maps used to verify the performance of different PhU methods. The coherence of the mining subsidence deformation centers is poor, which will have a more obvious impact on the PhU. From the PhU results of area 1, it is observable that the traditional model-driven PhU methods in the edge area of mining subsidence can obtain relatively ideal results. Nonetheless, noticeable PhU errors are present in the areas of phase discontinuity. Among the traditional model-driven PhU methods, only branch-cut can obtain a small amount of deformation phase, and other methods unable to obtain accurate PhU results. However, the deep learning PhU methods of DLPU, PUNet, and MMPhU-Net can still obtain satisfactory results in the areas of subsidence deformation centers, which can better reflect the real situation of subsidence. The deformation center of subsidence in area 2 has obvious interferometric fringe aliasing phenomenon. Therefore, the unwrapped results of traditional model-driven methods cannot obtain ideal PhU in the deformation center of subsidence. DLPU and PUNet can obtain better PhU results than traditional model-driven methods. However, comparing the subsidence deformation area, both methods have different degrees of PhU errors. MMPhU-Net can take into account the advantages of different network models. Therefore, MMPhU-Net can obtain favorable results even in the subsidence center area with large-gradient changes. The fringes of the mining subsidence deformation area 3 are relatively clear.

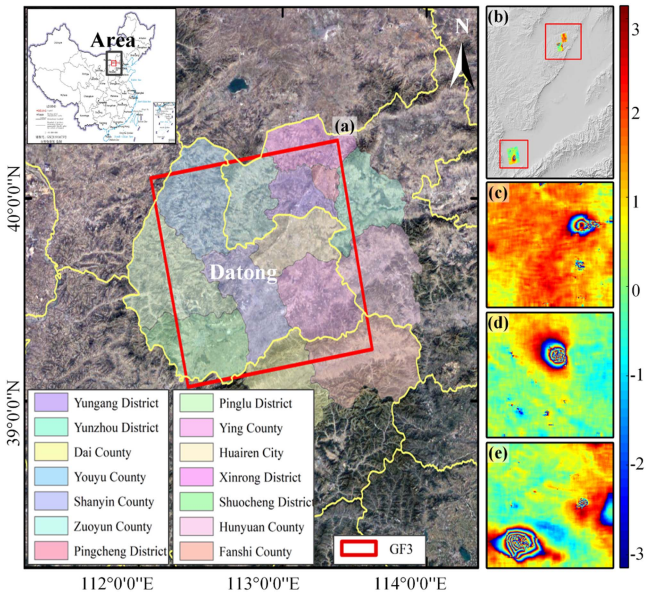

Fig. 7. Distribution map of realistic data experiment data. (a) Red rectangle indicates the coverage of the GF-3 data used for validation. (b) DEM of the red rectangle. (c)–(e) Filtered interferograms in the red rectangles of (b).

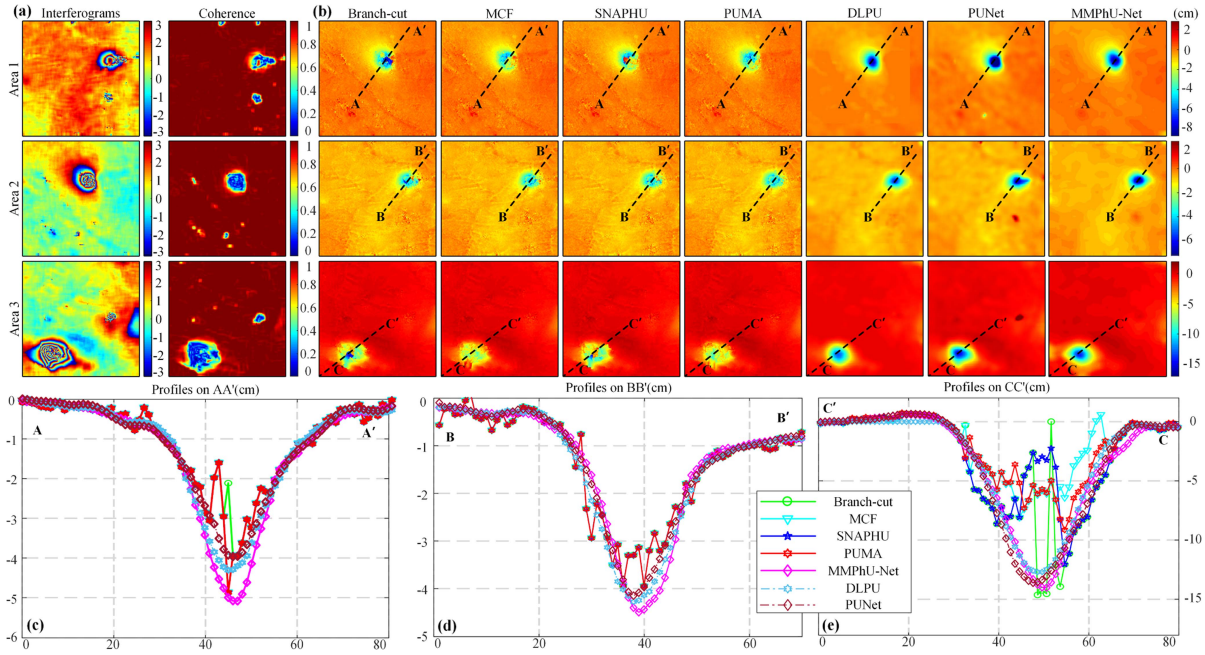

Fig. 8. Experimental results on real data. (a) Interferograms and coherence maps of different samples. (b) Deformations obtained by different PhU methods. (c)–(e) Profiles through the deformation center.

However, due to the influence of large-gradients or high-noise, the fringes of the filtered interferogram are more complicated. Based on the PhU results obtained from the branch-cut method, it is evident that a small amount of deformation phase in the mining subsidence center can be obtain, however, it still produces obvious PhU errors. The PhU errors of MCF, SNAPHU and PUMA results in area 3 are more obvious. Especially in the deformation centers, these three methods can hardly obtain deformation results. DLPU can better reflect the characteristics of deformation. However, similar to the simulation data results, DLPU still has obvious phase loss in the center of subsidence deformation. PUNet and MMPhU-Net method can better obtain the deformation of subsidence centers, and can more accurately reflect the actual situation of mining subsidence deformation. We obtained profiles through the centers of the three mining subsidence areas. Fig. 8(c) is the profiles of the different PhU methods results in area 1. It is evident that model-driven PhU methods can obtain satisfactory unwrapped results along the edges of subsidence areas; nevertheless, these methods fail to obtain satisfactory results in the subsidence center. DLPU and PUNet can obtain part of the deformation amount at the center of deformation. However, similar to the model data results, their PhU results will produce obvious phase loss at the center of deformation. In contrast, the profile of MMPhU-Net can better describe the deformation characteristics of the mining. Therefore, it can be proved that MMPhU-Net not only can solve the PhU problem in the easy area, but also can obtain satisfactory PhU results in the large-gradient deformation area. From Fig. 8(d), we can see the results of traditional model-driven methods are relatively similar, and these methods obviously produce losses in the deformation center of subsidence. Similar to the first experiment, both DLPU and PUNet can obtain ideal results. However, a single deep learning network model is prone to underestimation, resulting in obvious phase loss at the center of the deformation. However, the MMPhU-Net method can still accurately reflect the deformation of the coal mining area. The profiles of MCF, SNAPHU, and PUMA in Fig. 8(e) are relatively similar, with noticeable errors apparent in the central subsidence areas. The profile of branch-cut coincides with the profile of MMPhU-Net with a small number of points, but branch-cut still has obvious loss phenomenon. Similar to the previous results, the general trend of the PhU results of DLPU and PUNet is similar to that of MMPhU-Net. However, phase loss occurs in the subsidence center area. MMPhU-Net still can better obtain the basic characteristics of deformation.

V. Conclusion and Discussion

A novel PhU method based on multilearning network model fusion named MMPhU-Net is proposed. This method can obtain the deformation center in mining area, especially the problem of obtaining the deformation center caused by large-gradient changes. In this article, the fusion model network is composed of U-Net and SegNet, and trained the fused multimodel learning network by using the interferograms as the input and the k distribution maps as the output. Finally, the k distribution maps of the deformation area are obtained through the trained multimodel fusion network, and the final deformation phase is obtained by combining a TSF method. We use three sets of simulated data to analyze the MMPhU-Net. The results prove that MMPhU-Net can achieve better results than commonly used PhU methods.

From the three sets of realistic GaoFen-3 SAR substance deformation data experiment, in the actual data processing process, the fringes in the center area of mining substance deformation are obviously damaged. Existing PhU methods are prone to unwrapped errors. By expanding the deformation area, it can

be seen that the existing methods have produced obvious PhU errors. Although branch-cut can obtain a small amount of deformation of the subsidence deformation centers, it still produces obvious errors due to high-noise and large-gradient changes. From the profiles through the centers of the subsidence, it can be seen that the existing PhU methods can obtain good results in the deformation edge areas, however, there are obvious errors in the deformation centers, which caused serious deformation loss phenomenon. However, the MMPhU-Net proposed in this article not only achieves the same results as the existing methods in the deformation edge areas, but also achieves ideal unwrapped results in the deformation centers.

Semantic segmentation model has gradually become the leader in the field of weakly supervised classification-pixel segmentation, and with the introduction of residual module, attention mechanism and other structures, dozens of network variants have evolved. But not all of them are suitable for the research content of this manuscript. In the process of selecting the basic model, this article mainly considers the following two aspects: First, the overall computational complexity should not be too high, and the model parameters should be kept at a low level to facilitate subsequent algorithm processing and system deployment. Second, the size and shape of the k to be detected on the influence are different. The model needs to extract multiscale features of the target region, and retains high gradient edge detection accuracy. Based on the above two aspects, we decide to choose U-Net and SegNet as our basic network structures, and improve the training effect through Adboosting and the final extraction effect through postprocessing.

REFERENCES

[1] H. Yu, Z. Li, and Z. Bao, "A cluster-analysis-based efficient multibaseline phase-unwrapping algorithm," *IEEE Trans. Geosci. Remote Sens.*, vol. 49, no. 1, pp. 478–487, Jan. 2011.

[2] C. Noviello et al., "Monitoring buildings at landslide risk with SAR: A methodology based on the use of multipass interferometric data," *IEEE Geosci. Remote Sens. Mag.*, vol. 8, no. 1, pp. 91–119, Mar. 2020.

[3] H. Yu, H. Lee, T. Yuan, and N. Cao, "A novel method for deformation estimation based on multibaseline InSAR phase unwrapping," *IEEE Trans. Geosci. Remote Sens.*, vol. 56, no. 9, pp. 5231–5243, Sep. 2018.

[4] W. Liu, Z. Bian, Z. Liu, and Q. Zhang, "Evaluation of a cubature Kalman filtering-based phase unwrapping method for differential interferograms with high noise in coal mining areas," *Sensors*, vol. 15, no. 7, pp. 16336–16357, Jul. 2015.

[5] J. Yao, X. Yao, Z. Wu, X. Liu, and G. Diraco, "Research on surface deformation of ordos coal mining area by integrating multitemporal D-InSAR and offset-tracking technology," *J. Sensors*, vol. 2021, no. 4, pp. 1–14, Apr. 2021.

[6] Y. Yang, A. Pepe, M. Manzo, F. Casu, and R. Lanari, "A region-growing technique to improve multi-temporal DInSAR interferogram phase unwrapping performance," *Remote Sens. Lett.*, vol. 4, no. 10, pp. 988–997, Aug. 2013.

[7] A. S. Khwaja and M. Cetin, "Improved DInSAR time-series reconstruction in the presence of phase unwrapping errors using Huber-norm," *Inst. Eng. Technol. Radar, Sonar Navigation*, vol. 13, no. 7, pp. 1063–1073, Jul. 2019.

[8] Y. Gao, S. Zhang, T. Li, Q. Chen, X. Zhang, and S. Li, "Refined two-stage programming approach of phase unwrapping for multi-baseline SAR interferograms using the unscented Kalman filter," *Remote Sens.*, vol. 11, no. 2, pp. 119–139, Jan. 2019.

[9] H. Yu, H. Lee, N. Cao, and Y. Lan, "Optimal baseline design for multi-baseline InSAR phase unwrapping," *IEEE Trans. Geosci. Remote Sens.*, vol. 57, no. 8, pp. 5738–5750, Aug. 2019.

[10] H. Yu, Y. Lan, Z. Yuan, J. Xu, and H. Lee, "Phase unwrapping in InSAR: A review," *IEEE Geosci. Remote Sens. Mag.*, vol. 7, no. 1, pp. 40–58, Mar. 2019.

[11] X. Diao, K. Wu, Y. Xu, D. Zhou, and R. Chen, "Prediction-based phase unwrapping for differential interferograms of coal mining areas using a stochastic medium model," *Remote Sens. Lett.*, vol. 9, no. 5, pp. 478–487, Feb. 2018.

[12] C. De Luca, G. Onorato, F. Casu, R. Lanari, and M. Manunta, "A genetic algorithm for phase unwrapping errors correction in the SBAS-DInSAR approach," in *Proc. IEEE Int. Geosci. Remote Sens. Symp.*, 2019, pp. 266–269.

[13] Z. Yang, B. Xu, Z. Li, L. Wu, and J. Zhu, "Prediction of mining-induced kinematic 3-D displacements from InSAR using a Weibull model and a Kalman filter," *IEEE Trans. Geosci. Remote Sens.*, vol. 60, Feb. 2021, Art. no. 4500912.

[14] H. X. Wu, H. Wang, X. R. Huang, P. Carolina, and Z. X. Yang, "Improving the coherence of interferograms of mining subsidence by oversampling," *J. Guangdong Univ. Technol.*, vol. 32, no. 3, pp. 123–126, Aug. 2015.

[15] A. H.-M. Ng, L. Ge, Z. Du, S. Wang, and C. Ma, "Satellite radar interferometry for monitoring subsidence induced by longwall mining activity using Radarsat-2, Sentinel-1 and ALOS-2 data," *Int. J. Appl. Earth Observ. Geoinf.*, vol. 61, pp. 92–103, Sep. 2017.

[16] D. Ou, K. Tan, Q. Du, Y. Chen, and J. Ding, "Decision fusion of D-InSAR and pixel offset-tracking for coal mining deformation monitoring," *Remote Sens.*, vol. 10, no. 7, Jul. 2018, Art. no. 1055.

[17] C. Zhao, Z. Lu, and Q. Zhang, "Time-series deformation monitoring over mining regions with SAR intensity-based offset measurements," *Remote Sens. Lett.*, vol. 4, no. 5, pp. 436–445, Dec. 2012.

[18] Y. Chen, Y. Tong, and K. Tan, "Coal mining deformation monitoring using SBAS-InSAR and offset-tracking a case study of Yu county China," *IEEE J. Sel. Topics Appl. Earth Observ. Remote Sens.*, vol. 13, pp. 6077–6087, Oct. 2020.

[19] J. Huang, K. Deng, H. Fan, S. Lei, S. Yan, and L. Wang, "An improved adaptive template size pixel-tracking method for monitoring large-gradient mining subsidence," *J. Sensors*, vol. 2017, pp. 1–11, Sep. 2017.

[20] J. Zhu, Z. Yang, and Z. Li, "Recent progress in retrieving and predicting mining-induced 3D displacements using InSAR," *Acta Geodaetica et Cartographica Sinica*, vol. 48, no. 2, pp. 135–144, Feb. 2019.

[21] C. Bingqian, D. Kazhong, F. Hongdong, and H. Ming, "Large-scale deformation monitoring in mining area by D-InSAR and 3D laser scanning technology integration," *Int. J. Mining Sci. Technol.*, vol. 23, no. 4, pp. 555–561, Jul. 2013.

[22] Z. Yang, J. Zhu, Z. Li, Y. Wang, and G. Chen, "Analysing the law of dynamic subsidence in mining area by fusing InSAR and leveling measurements," *Int. Arch. Photogramm., Remote Sens. Spatial Inf. Sci.*, vol. 40, pp. 163–166, Jul. 2013.

[23] C. Jiang, L. Wang, X. Yu, S. Chi, T. Wei, and X. Wang, "DPIM-based InSAR phase unwrapping model and a 3D mining-induced surface deformation extracting method: A case of Huainan mining area," *Korean Soc. Civil Engineers J. Civil Eng.*, vol. 25, no. 24, pp. 654–668, Dec. 2020.

[24] Z. Yang, Z. Li, J. Zhu, H. Yi, J. Hu, and G. Feng, "Deriving dynamic subsidence of coal mining areas using InSAR and logistic model," *Remote Sens.*, vol. 9, no. 2, pp. 125–144, Jan. 2017.

[25] H. Fan, W. Gu, Y. Qin, J. Xue, and B. Chen, "A model for extracting large deformation mining subsidence using D-InSAR technique and probability integral method," *Trans. Nonferrous Met. Soc. China*, vol. 24, no. 4, pp. 1242–1247, Apr. 2014.

[26] Y. Dai, A. H.-M. Ng, H. Wang, L. Li, L. Ge, and T. Tao, "Modeling-assisted InSAR Phase-unwrapping method for mapping mine subsidence," *IEEE Geosci. Remote Sens. Lett.*, vol. 18, no. 6, pp. 1059–1063, Jun. 2021.

[27] Y. Gao, S. Zhang, T. Li, Q. Chen, S. Li, and P. Meng, "Adaptive unscented Kalman filter phase unwrapping method and its application on gaofen-3 interferometric SAR data," *Sensors*, vol. 18, no. 6, Jun. 2018, Art. no. 1793.

[28] Y. Gao et al., "A phase slicing 2-D phase unwrapping method using the L1-norm," *IEEE Geosci. Remote Sens. Lett.*, vol. 19, Sep. 2020, Art. no. 4002805.

[29] H. Yu and Y. Lan, "Robust two-dimensional phase unwrapping for multi-baseline SAR interferograms a two-stage programming approach," *IEEE Trans. Geosci. Remote Sens.*, vol. 54, no. 9, pp. 5217–5225, Sep. 2016.

[30] H. Yu and X. Hu, "Knowledge-aided InSAR phase unwrapping approach," *IEEE Trans. Geosci. Remote Sens.*, vol. 60, May 2021, Art. no. 5209508.

[31] Y. Gao et al., "Two-dimensional phase unwrapping method using a refined D-LinkNet-based unscented Kalman filter," *Opt Lasers Eng.*, vol. 152, no. 1, May 2022, Art. no. 106948.

[32] L. Zhou, H. Yu, Y. Lan, and M. Xing, "Artificial intelligence in interferometric synthetic aperture radar phase unwrapping: A review," *IEEE Geosci. Remote Sens. Mag.*, vol. 9, no. 2, pp. 10–28, Jun. 2021.
[33] L. Zhou, H. Yu, and Y. Lan, "Deep convolutional neural network-based robust phase gradient estimation for two-dimensional phase unwrapping using SAR interferograms," *IEEE Trans. Geosci. Remote Sens.*, vol. 58, no. 7, pp. 4653–4665, Jul. 2020.
[34] G. E. Spoorthi, R. K. S. S. Gorthi, and S. Gorthi, "PhaseNet 2.0 phase unwrapping of noisy data based on deep learning approach," *IEEE Trans. Image Process.*, vol. 29, pp. 4862–4872, Mar. 2020.
[35] L. Zhou, H. Yu, V. Pascazio, and M. Xing, "PU-GAN: A one-step 2-D InSAR phase unwrapping based on conditional generative adversarial network," *IEEE Trans. Geosci. Remote Sens.*, vol. 60, Jan. 2022, Art. no. 5221510.
[36] Z. Wu, T. Wang, Y. Wang, R. Wang, and D. Ge, "Deep learning for the detection and phase unwrapping of mining-induced deformation in large-scale interferograms," *IEEE Trans. Geosci. Remote Sens.*, vol. 60, Oct. 2021, Art. no. 5216318.
[37] Z. Wu, T. Wang, Y. Wang, R. Wang, and D. Ge, "Deep-learning-based phase discontinuity prediction for 2-D phase unwrapping of SAR interferograms," *IEEE Trans. Geosci. Remote Sens.*, vol. 60, Oct. 2021, Art. no. 5216516.
[38] L. Zhou, H. Yu, Y. Lan, S. Gong, and M. Xing, "CANet: An unsupervised deep convolutional neural network for efficient cluster-analysis-based multibaseline InSAR phase unwrapping," *IEEE Trans. Geosci. Remote Sens.*, vol. 60, Sep. 2021, Art. no. 5212315.
[39] L. Zhou, H. Yu, Y. Lan, and M. Xing, "Deep learning-based branch-cut method for InSAR two-dimensional phase unwrapping," *IEEE Trans. Geosci. Remote Sens.*, vol. 60, Aug. 2021, Art. no. 5209615.
[40] A. Garcia-Garcia, S. Orts-Escolano, S. Oprea, V. Villena-Martinez, and J. Rodríguez, "A review on deep learning techniques applied to semantic segmentation," Apr. 2017, *arXiv: 1704.06857*.
[41] M. Angulakshmi and M. Deepa, "A review on deep learning architecture and methods for MRI brain tumor segmentation," *Curr. Med. Imag.*, vol. 17, no. 6, pp. 695–706, 2021.
[42] O. Ronneberger, P. Fischer, and T. Brox, "U-Net: Convolutional networks for biomedical image segmentation," in *Medical Image Computing and Computer-Assisted Intervention*, Berlin, Germany: Springer, 2015; pp. 234–241.
[43] V. Badrinarayanan, A. Kendall, and R. Cipolla, "SegNet: A deep convolutional encoder-decoder architecture for image segmentation," *IEEE Trans. Pattern Anal. Mach. Intell.*, vol. 39, no. 12, pp. 2481–2495, Dec. 2017.
[44] J. Yao et al., "Cloud detection of GF-7 satellite laser footprint image," *Inst. Eng. Technol. Image Process.*, vol. 15, no. 10, pp. 2127–2134, Aug. 2021.
[45] X. Tang, J. Yao, J. Chen, G. Li, and W. Zhang, "Multimodel fusion method for cloud detection in satellite laser footprint images," *IEEE Geosci. Remote Sens. Lett.*, vol. 19, 2022, Art. no. 6513905.
[46] B. Pang, E. Nijkamp, and Y. N. Wu, "Deep learning with TensorFlow: A review," *J. Educ. Behav. Statist.*, vol. 45, no. 2, pp. 227–248, Sep. 2019.
[47] Y. Gao, S. Zhang, T. Li, L. Guo, Q. Chen, and S. Li, "A novel two-step noise reduction approach for interferometric phase images," *Opt. Lasers Eng.*, vol. 121, pp. 1–10, Oct. 2019.
[48] K. Wang, Y. Li, Q. Kemao, J. Di, and J. Zhao, "One-step robust deep learning phase unwrapping," *Opt. Exp.*, vol. 27, no. 10, pp. 15100–15115, May 2019.

Yandong Gao received the B.Sc. and M.Sc. degrees in survey and mapping engineering from University of Science and Technology Liaoning, Anshan, in 2013 and 2016, respectively, and the Ph.D. degree in geodesy and surveying engineering from the School of Environment Science and Spatial Informatics, China University of Mining and Technology, Xuzhou, China, in 2019.

He is currently an Associate Professor with the School of Environment Science and Spatial Informatics, China University of Mining and Technology, Xuzhou, China. His research interests include the fields of interferometric phase filtering, phase unwrapping, and synthetic aperture radar interferometry signal processing and applications.

Jiaqi Yao received the B.Sc. degree in surveying and mapping engineering from North China University of Science and Technology, Tangshan, China, in 2017, the M.Sc. degree in photogrammetry and remote sensing from Liaoning Technical University, Fuxin, China, in 2019, and the Ph.D. degree in photogrammetry and remote sensing from College of Geomatics, Shandong University of Science and Technology, Qingdao, China, in 2022.

He is currently a Research Assistant with the Tianjin Normal University. His research interests include the application of deep learning in satellite LiDAR.

Nanshan Zheng was born in Anqing, China, in 1974. He received the B.Sc. and M.Sc. degrees in geodesy and surveying engineering from the China University of Mining and Technology, Xuzhou, China, in 1995 and 1998, respectively, and the Ph.D. degree in urban environment from Kyoto University, Kyoto, Japan, in 2009.

He is currently a Professor with the School of Environmental Science and Spatial Informatics, China University of Mining and Technology, where he is currently the Dean. He has authored or coauthored more than 60 peer-reviewed journal articles or conference papers. His recent research interests include global navigation satellite system-reflectometry, remote sensing, and risk assessment of environmental disasters.

Shijin Li received the Ph.D. degree in geodesy and surveying engineering and B.Sc. degree in survey and mapping engineering from China University of Mining and Technology, Xuzhou, China, in 2022 and 2017.

He is currently a Post-Doctoral Research Fellow with the School of Environment Science and Spatial Informatics, China University of Mining and Technology, Xuzhou, China. His current research interests include the fields of interferometric synthetic aperture radar phase filtering, phase unwrapping, multitemporal InSAR data processing, and deformation measurement.

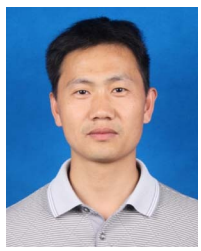

Hefang Bian received the B.Sc. degree in surveying and mapping engineering from the Anhui University of Science and Technology, Huainan, China, in 2006, and the M.Sc. and Ph.D. degrees in survey and mapping engineering from China University of Mining and Technology, Xuzhou, China, in 2009 and 2013.

He is currently a Lecturer with the School of Environment Science and Spatial Informatics at the China University of Mining and Technology. His research interests include GNSS and LiDAR.

Yu Tian received the Ph.D. degree in geodesy and surveying engineering and B.Sc. degree in survey and mapping engineering from China University of Mining and Technology, Xuzhou, China, in 2022 and 2016.

He is currently a Post-Doctoral Research Fellow with the School of Environment Science and Spatial Informatics, China University of Mining and Technology, Xuzhou, China. He has published several SCI articles in *Journal of Soils and Sediments, Remote Sensing, International Journal of Environmental Research* and *Public Health*, and other journals. His research interests include environmental remote sensing and LiDAR point cloud processing algorithms.